Microautonomous Robotic Ostraciiform (MARCO): Hydrodynamics, Design, and Fabrication

Parasar Kodati, Jonathan Hinkle, Aaron Winn, and Xinyan Deng

***Abstract*—Boxfish with multiple fins can maneuver in confined spaces with a near zero turning radius, and it has been found that its unusual boxy shape is responsible for a self-correcting mechanism that makes its trajectories immune to water disturbances. The microautonomous robotic ostraciiform aims to apply these features in a novel underwater vehicle design. Miniature underwater vehicles with these characteristics have a variety of applications, such as environmental monitoring, ship wreck exploration, inline pipe inspection, forming sensor networks, etc. This paper presents the research leading to the design and fabrication of a robotic ostraciiform. Tail fin hydrodynamics have been investigated experimentally using robotic flapper mechanisms to arrive at a caudal fin shape with optimal-shape-induced flexibility. Fluid simulation studies were utilized to arrive at the body shape that can result in a self-correcting vorticity generation. Finally, the robotic ostraciiform prototype was designed based on the previous results. The ostracifform locomotion is implemented with a pair of 2 DOF pectoral fins and a single DOF tail fin. The finalized body shape of the robot is produced by 3-D prototyping two separate halves.**

***Index Terms*—Body shape design, boxfish, flapping fin hydrodynamics, robotic ostraciiform.**

I. Introduction

AUTONOMOUS underwater vehicles (AUVs) are being extensively used for a variety of applications ranging from environmental monitoring to oil and gas exploration [1]. However, these AUVs are not suitable for applications where the vehicle has to explore confined spaces like ship wrecks or oil pipe lines, where maneuverability and stability are more important than the speed. Tasks such as these call for designs that are small, maneuverable, and precisely controlled. The present paper is a step toward realizing such microunderwater vehicles (MUVs). In this paper, we present the research (see Fig. 1, bioinspired design process) leading to the design and fabrication of microautonomous robotic ostraciiform (MARCO) [2]. The design is based on experimental flapping fin hydrodynamic results [3] to choose an optimal fin shape-flexure combination and simulation studies conducted to arrive at a self-stabilizing body shape [4].

Manuscript received February 2, 2007; revised October 16, 2007. This paper was recommended by Associate Editor P. Dario and Editor F. Park upon evaluation of the reviewers' comment.

P. Kodati was with the University of Delaware, Newark, DE 19716-3140 USA. He is now with the Mathworks Inc., Natick, MA 01760 USA (e-mail: parasar.kodati@gmail.com).

J. Hinkle was with the Department of Mechanical Engineering, University of Delaware, Newark, DE 19716-3140 USA. He is now with the the International Linear Collider (ILC), Dover, DE 19946-3140 USA (e-mail: jhinkle@udel.edu).

A. Winn and X. Deng are with the Department of Mechanical Engineering, University of Delaware, Newark, DE 19716-3140 USA (e-mail: agwinn@udel.edu; deng@udel.edu).

Color versions of one or more of the figures in this paper are available online at http://ieeexplore.ieee.org.

Digital Object Identifier 10.1109/TRO.2008.915446

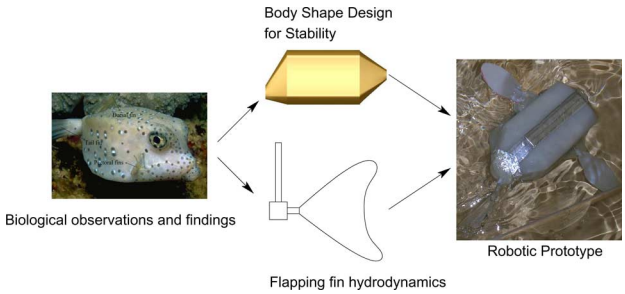

Fig. 1. Bioinspired design process.

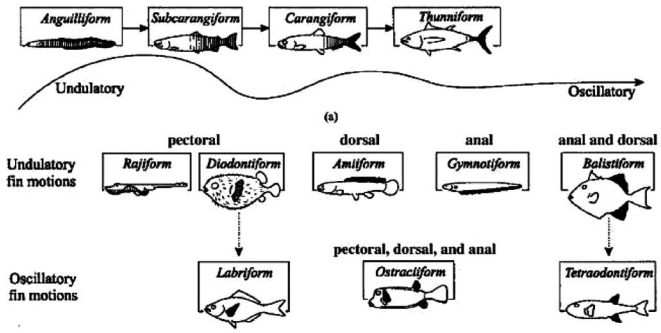

Fig. 2. Fish classification based on swimming styles originally appeared in [6] and modified in [7].

A. Overview of Biomimetic Underwater Robots/Vehicles

In order to improve the performance of AUVs in terms of efficiency and maneuverability, many researchers have proposed biomimetic propulsion systems that swim by using flapping fins rather than rotary thrusters. The effort to exploit unique locomotion characteristics found in a variety of fish for use in underwater robots includes understanding the physics of flapping fin propulsion, designing electromechanical architecture (motors and mechanisms) that can mimic the motion of the appendages, and formulating the control structure, so that the robot can effectively "swim." In the following paragraphs, the authors present a brief outline of the main swimming styles found in fish and their robotic counterparts. Sfakiotakis *et al*. [5] present a good review of fish swimming modes targeted at roboticists interested in an aquatic locomotion.

Fig. 2 shows a classification scheme of fish locomotion mechanisms. It was originally presented in [6] and was modified in [7]. The three main swimming styles are characterized by undulatory body motion, undulatory fin motion, and oscillatory fin motion. A more traditional classification is the one proposed by Breder [8] that broadly identifies two styles of swimming: one is body and/or caudal fin (BCF) locomotion, and the other

1552-3098/$25.00 © 2008 IEEE

is median and/or paired fin (BMP) locomotion. Fish classes that use varying degrees of body undulation and/or caudal fin oscillations for thrust generation are examples of the BCF swimming, and fish that use paired fins like the left and right pectoral fins, dorsal, and ventral pelvic fins for thrust generation are classified under the MPF swimming style.

The undulatory to oscillatory motion continuum (see the first row of fish in Fig. 2) has been the primary focus of the fish–robot design. An anguilliform has the maximum undulatory motion, and can be characterized by a transverse-wave traveling through the length of the entire body. In carangiform through thunniform, the body undulatory motion is confined only to the third posterior. The ostraciiform was initially believed to be at the oscillatory end with an oscillating tail fin for propulsion. However, recent biological observations indicate that the ostraciiform's multiple fin structure does much more than "sculling the tail" [9]: boxfish use a variety of fins in different gaits depending on the propulsion speed, a behavior that enables them to minimize the recoil movement (unwanted deviation that results from flapping) and maintain a more constant energy usage. Most recently, Bartol *et al*. [10], [11] have found that a body shape with keel structures plays an important role in correcting the body orientation in the presence of disturbances by shedding counter rotating vortices.

Massachusetts Institute of Technology's (MIT) Robotuna, built by Triantafyllou's group [12], marked the beginning of the biomimetic approach in underwater vehicles. The design is based on the carangiform locomotion. Barrett *et al*. [13] demonstrated that the highly articulated robotic fish experienced less drag with an undulatory motion than that seen without the body undulation. Zhu *et al*. [14] from the same group also identified a vorticity control phenomenon, which explains the interaction of the vortices shed by the undulating body and the ones in the wake shed by the tail fin. Such interaction of the body with the wake was also shown to reduce the muscle activity in fish [15].

The anguilliform requires a greater amount of body undulation, and thus, more DOFs must be connected in series to form a robot design of this type. McIsaac and Ostrowski [16] studied the motion planning and the control of a serial chain robotic eel (REEL). They have generated gaits (time functions of the joint angles) for the straight and turning motions of three-link and five-link robots. MacIver *et al*. [17] presented some aspects of underwater vehicle design in the areas of sensing and motion mechanisms of a knifefish in [18].

The Biologically Inspired Robotics Group (BIRG) at the Ecole Polytechnique Federale de Lausanne (EPFL) presented a swimming and crawling robot, BoxyBot [19], that is "loosely inspired by the boxfish." The focus there was to mimic the boxfish-like switching of swimming modes under different speed ranges. Prior to this paper was Berkeley's centimeter microswimming robot, which realized three flapping fins using the piezoelectric actuation. More recently, biologically inspired robot designs include Basilisk lizard-like water running robot [20].

Currently, a new class of "biorobotic" underwater vehicles based on the biomimetic principles of flapping foils are being designed. These platforms do not necessarily mimic the locomotion style of a particular fish class, but employ fin designs and motion kinematics that are the result of experimental and computational fluid mechanics work. Licht *et al*. [21] presented the design of a vehicle platform with four heaving and pitching foils. A team of ocean engineers, fluid mechanists, and biologists proposed a concept vehicle, taking advantage of high-efficiency foils in combination with articulated pectoral fins with rays for enhanced maneuverability [22]. Pulsatile jet formation loosely inspired by squid is presented in [23]. Kato's Bass III [24] is the latest 3 DOF pectoral-fin-based vehicle designed for low-speed precise maneuvering.

Bandyopadhyay [25] presented a comprehensive review of approaches on various fronts of biomimetic underwater vehicle technology like high lift generating fin hydrodynamics, vehicle maneuverability using pectoral fins, muscle-like actuators, and neuroscience-based control.

The present paper is organized as follows. Section I briefly describes the experimental setup for studying flapping fin hydrodynamics and presents the results of the shape-induced flexibility of the caudal fin. An optimally flexible shape is arrived for the prototype and the force generation is characterized in the form of an empirical model relating the forces to the flapping parameters. Section II presents the modeling of boxfish-like engineering shapes using computer-aided design (CAD) tools, incorporating key morphological features that are responsible for self-correcting vorticity generation as explained by Bartol *et al*. in [11]. Fluid flow simulation was used to verify the self correcting vorticity effect on these models and arrive at a shape for the robotic prototype. Finally, in Section III the design and fabrication of the robotic prototype is presented.

Part I: Flapping Fin Hydrodynamics

Recently, the optimization of flapping fin performance for the purpose of deployment in biorobotic underwater vehicles has received considerable attention. Triantafyllou *et al*. [26] have used heaving and pitching foils to study the propulsive performance, and have found that there is an optimal Strouhal number range: 0.2–0.5, where efficiency is at a maximum. This is also the range in which a majority of fish and Cetaceans swim. More recently, Prempraneerach *et al*. [27] studied foils of different chordwise flexibilities, but with identical geometries and heaving/pitching kinematics. Their studies yielded an optimal level of flexibility that significantly increased the efficiency. Kato and Liu [28] found that, for a pectoral-fin-based underwater vehicle, a *flapping* (dorso-ventral flapping with fin rotation, similar to the heaving and pitching case) motion is more efficient in thrust production at higher speeds than a *rowing* (fore-aft flapping with fin rotation) motion, and *rowing* is more effective than flapping in still water. This is a result that Walker and Westneat [29] predicted using a hydrodynamic simulation based on fish data. Triantafyllou *et al*. present a comprehensive review of the experimental work on biomimetic foils in [30].

The present study and experiments focus on ostraciiform fin force generation and shape-induced flexing. The propulsion hydrodynamic forces on the oscillating caudal fin are studied by varying the fin morphological parameters and fin motion kinematics. These parameters include the Strouhal number and fin

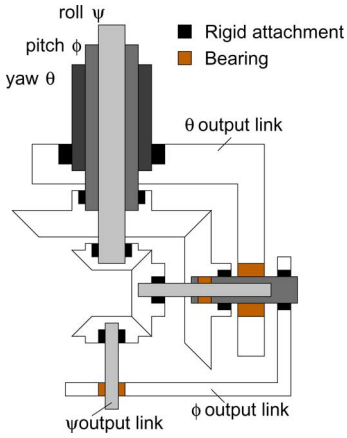

Fig. 3. Robotic flapper and force measurement setup.

stiffness due to the material flexibility and geometry. The immediate goal of the study is to arrive at the optimal fin shape and motion parameters for the MUV design, and also to use the results in modeling the hydrodynamics, to the required complexity, for use in the controller design, and system simulation. Toward this end, a robotic flapper was built and used to measure the forces and moments generated for a set of fin motion, material, and shape parameters.

II. Experimental Setup

A robotic flapper, inspired by the Robofly [31], was designed to generate fin motion in three independent rotational DOFs. A bevel gear wrist mechanism was used to transmit the motion of coaxial drive shafts to the fin, as shown in Fig. 3. The mechanism design allows a greater angular range of motion: the roll and yaw ranges do not have any limits, but the pitch angle is constrained to 45° in the upward direction. The compact size (1.5 in × 1.5 in × 1.25 in) of the wrist also does not generate any unwanted water disturbance that can affect the fin hydrodynamics. The drive shafts were powered by Maxon 16 mm dc brush motors with planetary gearheads and magnetic encoders. Gearhead reductions were 19:1 for yaw and pitch, and 84:1 for roll. All three motors have since been upgraded to 84:1 gearheads. The mechanism itself saw gear ratios (drive to driven) of 4:1 for roll, 8:1 for yaw, and 1:1 for pitch. The relatively small size of the wrist mechanism minimizes the fluid disturbance (see Fig. 3). The motors were driven from Simulink models, which use an additional toolbox provided by the control board manufacturer (Quanser consulting) to communicate with the hardware. PID controllers were used to run the motors at a high level of precision: up to a tenth of a degree. Motion commands from the computer were amplified by analog amplifier units (advanced motion control) running in torque mode, which directly controls the input current that the motor receives in order to perform a given motion. The flapper was fitted with an Amplifier Technologies, Inc., (ATI) Industrial Automation Nano17 force sensor. The sensor was manufactured with an oil-safe data and power cable, and is capable of measuring forces and moments along all three axes (see Fig. 4).

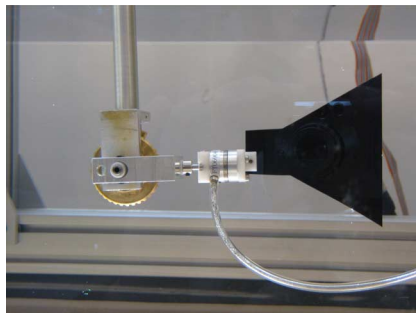

Fig. 4. Flapper setup with Nano 17 force sensor.

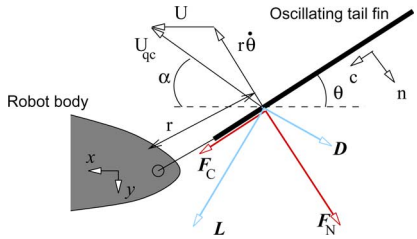

Fig. 5. Forces acting on the oscillating tail fin. Note that $D + L = F_C + F_N$.

The flapper was mounted on a linear stage that was driven by a National Electrical Manufacturers Association (NEMA) 34 stepper motor. A larger tank, measuring 60 in × 18 in × 16 in, was used to allow for linear motion. The tank was filled with refined paraffinic oil (relative density = 0.89 and dynamic viscosity = 3.03×10^{-3} Pa·s).

III. Optimal Flapping Fin Performance: Results and Discussion

The thrust (force in the direction of motion) produced by a flapping fin is a result of its interaction with the surrounding fluid. In the case of simple flapping (like the caudal fin of a boxfish in cruise mode), this interaction can lead to lift- and drag-based forces as well as added mass effects (resulting from the deceleration of fluid set in motion by previous strokes). Fig. 5 shows such forces acting on a foil. The lift component (L) of the total force (F) is a result of the periodic vortex shedding, while the rest of the components are due to drag (D).

A. Shape-Induced Flexibility

In this study, the shapes considered have a systematic progression of flexibility due to change in geometric parameters. A boxfish-like fin shape was used as the template to vary the fin geometry. To change the chordwise flexibility, the dimensions c_1 and c_2 have been varied while fixing the aspect ratio and the total area of the fin. This kind of parametric variation displaces the center of pressure of the fin, thus varying the degree of flexing. Fig. 6 shows the shape template that is used to obtain different tail fin shapes by varying c_1 and c_2. Four shapes (labeled S1–S4) from this continuum have been considered experimentally. Table I gives the geometric dimensions. The shapes were cut from 0.6-mm-thick delrin, 0.1-mm-thick polyimide, and 0.6-mm-thick polyethylene in order to look at them over a range

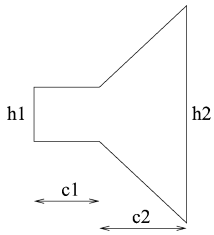

Fig. 6. Shape template used to vary the tail fin shape. See Table I for the values of c_1 and c_2 for the shapes considered.

TABLE I
SHAPE PARAMETERS FOR SHAPES S1 TO S4. SEE FIG. 6 FOR THE BASIC TEMPLATE OF THE BOXFISH-LIKE SHAPES

shape	c_1(in cm)	c_2(in cm)
S1	4.00	4.11
S2	3.01	4.57
S3	2.02	5.02
S4	1.00	5.50

of material stiffness. In fact, from a flexibility point of view, all 12 shapes (four profiles, three materials) form a continuum of flexural stiffness (EI) values, which have a strong correlation to the amount of flexing [32]. The term captures the elasticity (E, Young's modulus) of the fin material as well as the shape geometry (I, second moment of area) that together determine the fin's flexibility.

Each shape/material combination (with the exception of shape S1 of polyethylene) was flapped harmonically at frequencies ranging (in 0.1 Hz intervals) from 0.3 to 0.8 Hz, while being towed at a speed of 0.08 m/s. The Strouhal number is a nondimensional number that relates the forward velocity U to the flapping frequency f as

$$St = \frac{fw}{U} \tag{1}$$

where w is the wake width. In our case, w was treated as the width of a single fin stroke or

$$w = 2l \sin\theta_0 \tag{2}$$

where l is the total length of the fin and sensor (which is placed in between the fin and the base of rotation) and θ_0 is the angular amplitude.

We define the nondimensional thrust and drag coefficients as

$$C_T = \frac{2F_x}{\rho A U^2} \tag{3}$$

and

$$C_D = \frac{2F_y}{\rho A U^2} \tag{4}$$

where F_x and F_y are forward thrust and side way components of the force vector in the horizontal plane, ρ is the density of the fluid, A is the fin area, and η is defined as a measure of forward propulsive efficiency as

$$\eta = \kappa \frac{F_x U}{M_z \omega}. \tag{5}$$

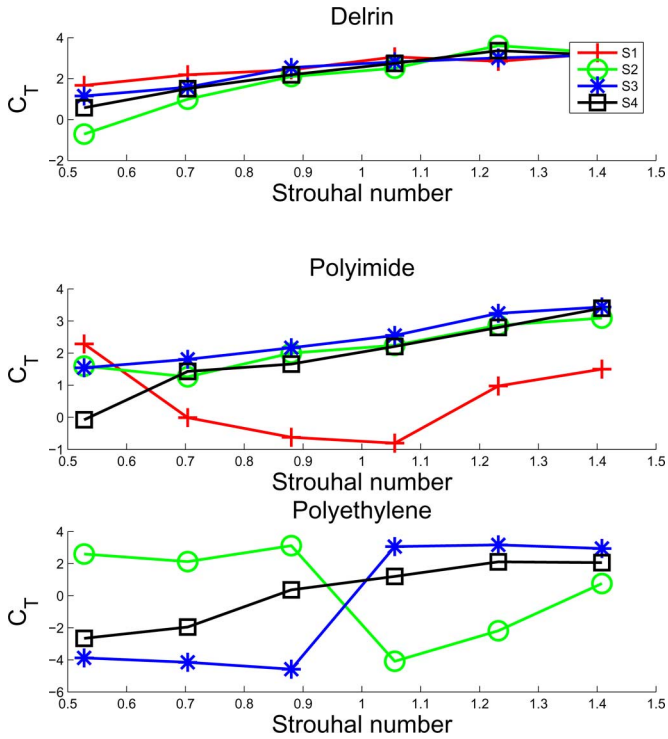

Fig. 7. Variation of C_T with frequency.

The denominator in (5) is taken as a measure of the torsional power required to drive the fin, where M_z is the moment measured by the force sensor, ω ($=2\pi f$) is the circular frequency of flapping, and κ is a nondimensional scaling constant.

Fig. 7 shows the variation of C_T over the four fin shapes of different materials (delrin, polyimide, and polyethylene). C_T increased with frequency except for shape S1 of polyimide and shape S2 of polyethylene fins. These two fins have a drastic drop in C_T after a certain frequency, and then, it begins to increase again. One possible explanation for this is that the force generation at lower frequencies for these two fins is viscous drag dominant. This effect drops after the Reynolds number, contribution of added mass, and pressure drag start to increase. Fig. 9 shows the force constitution found in the fish at different Reynolds numbers. The viscous effect drop can be seen clearly at Re $\sim$ 10. Fig. 8 shows the variation of η (measure of efficiency) with Strouhal number for all the fins used. The relatively more rigid delrin fins have peak efficiencies in the range of 0.8–1. Polyimide fins do not have much variation, for most part, with Strouhal number. The low efficiency of the polyethylene fins can, once again, be explained by high viscous drag.

The criteria for fin selection should be high values for C_T and η over a range of frequencies. The caudal fin flapping frequency is one of the key parameters that has to be changed to control the speed of the MUV. Thus, a fin with good thrust production and high efficiency over a range of frequencies is desirable. Shape S3 of polyimide is clearly the best choice as indicated by the C_T and η values.

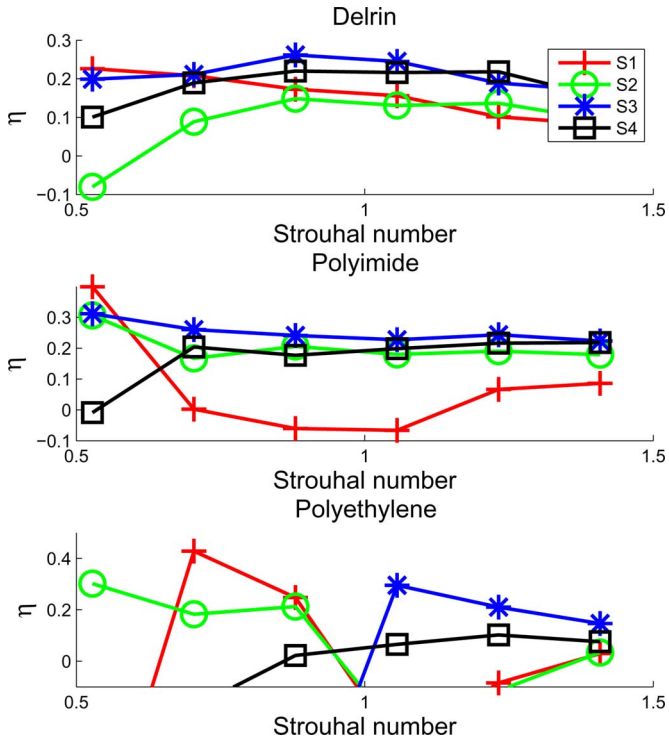

Fig. 8. Variation of η with frequency.

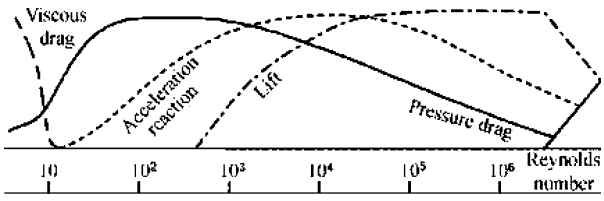

Fig. 9. "Relative contribution of momentum transfer mechanisms in swimming vertebrates as a function of Reynold's number," as appeared in Sfakiotakis *et al.*'s review [5].

B. Force Modeling

Fig. 5 shows the velocity and force diagrams and other kinematic parameters of the fin motion. With fin kinematics described by

$$\theta = \theta_0 \sin(2\pi f t) \tag{6}$$

the magnitude of the instantaneous total velocity vector U_{qc} at the quarter chord point, that is one fourth chord length, on the fin is given by

$$U_{qc} = \sqrt{r^2\dot{\theta}^2 + U^2 + 2r\dot{\theta}U\sin\theta} \tag{7}$$

where r is the distance between the revolute joint of the fin on the body and the quarter chord point of the fin. The instantaneous angle of attack α is given by

$$\alpha = \arctan\left(\frac{r\dot{\theta}\cos\theta}{U + r\dot{\theta}\sin\theta}\right). \tag{8}$$

TABLE II
ADDED MASS COEFFICIENTS FOR A THIN 2-D PLATE ([34])

μ_c	0
μ_n	$\rho\pi a^2$
μ_{nc}	0
$\mu_{c\omega}$	0
$\mu_{n\omega}$	$\rho\pi a^3$
μ_ω	$\frac{9}{8}\rho\pi a^4$

The time derivative of α is given by

$$\dot{\alpha} = \frac{-r^2\dot{\theta}^3 + Ur(\ddot{\theta}\cos\theta - \dot{\theta}^2\sin\theta)}{U^2 + (r\dot{\theta})^2 + 2Ur\dot{\theta}\sin\theta}. \tag{9}$$

The hydrodynamic forces were modeled in the coordinate frame fixed to the fin. This can be obtained by rotating the "body" coordinate axes attached to the linear stage, which sees the same forces as the MUV body, by an angle θ in the counterclockwise direction (see Fig. 5). The forces generated by the flapping fin–fluid interaction are due to lift, added mass, and drag components. The normal and chordwise forces on the fin in the fin coordinate system can be written as

$$F_n = F_n^l + F_n^{\text{am}} + F_n^d \tag{10}$$

$$F_c = F_c^l + F_c^{\text{am}} + F_c^d. \tag{11}$$

The components of the *lift* vector that is perpendicular to the total velocity vector can be written as

$$F_n^l = (C_L\sin\alpha)\rho A U_{qc}^2\cos(\alpha+\theta) \tag{12}$$

$$F_c^l = (C_L\sin\alpha)\rho A U_{qc}^2\sin(\alpha+\theta). \tag{13}$$

Here, the lift coefficient's dependence on the instantaneous angle of attack α has been separated using a sine function, which is a good approximation for 2-D unsteady foils [33]. It can be seen that this approximation also fits the measured forces well. Now, C_L is just a function of the shape and Reynolds number.

The *added mass effect* can be accounted for by using [34]

$$F_n^{\text{am}} = -\mu_{nc}\dot{U}_c - \mu_n\dot{U}_n - \mu_{nc}\ddot{\theta} - \dot{\theta}(\mu_c U_c + \mu_{nc}U_n + \mu_{c\omega}\dot{\theta}) \tag{14}$$

$$F_c^{\text{am}} = -\mu_c\dot{U}_c - \mu_{nc}\dot{U}_n - \mu_{c\omega}\ddot{\theta} + \dot{\theta}(\mu_{nc}U_c + \mu_n U_n + \mu_{n\omega}\dot{\theta}) \tag{15}$$

where the μ's are the added mass coefficients. For a flat plate, we can use the values in Table II.

The respective acceleration terms are given by

$$\dot{U}_n = \frac{1}{U_{qc}}r^2\dot{\theta}\ddot{\theta}\cos(\alpha+\theta) - U_{qc}(\dot{\alpha}+\dot{\theta})\sin(\alpha+\theta) \tag{16}$$

$$\dot{U}_c = -\frac{1}{U_{qc}}r^2\dot{\theta}\ddot{\theta}\sin(\alpha+\theta) - U_{qc}(\dot{\alpha}+\dot{\theta})\cos(\alpha+\theta). \tag{17}$$

The components of the *drag* vector that are along the total velocity vector can be written as

$$F_n^d = -C_D\rho A U_{qc}^2\sin(\alpha+\theta) \tag{18}$$

$$F_c^d = C_D\rho A U_{qc}^2\cos(\alpha+\theta). \tag{19}$$

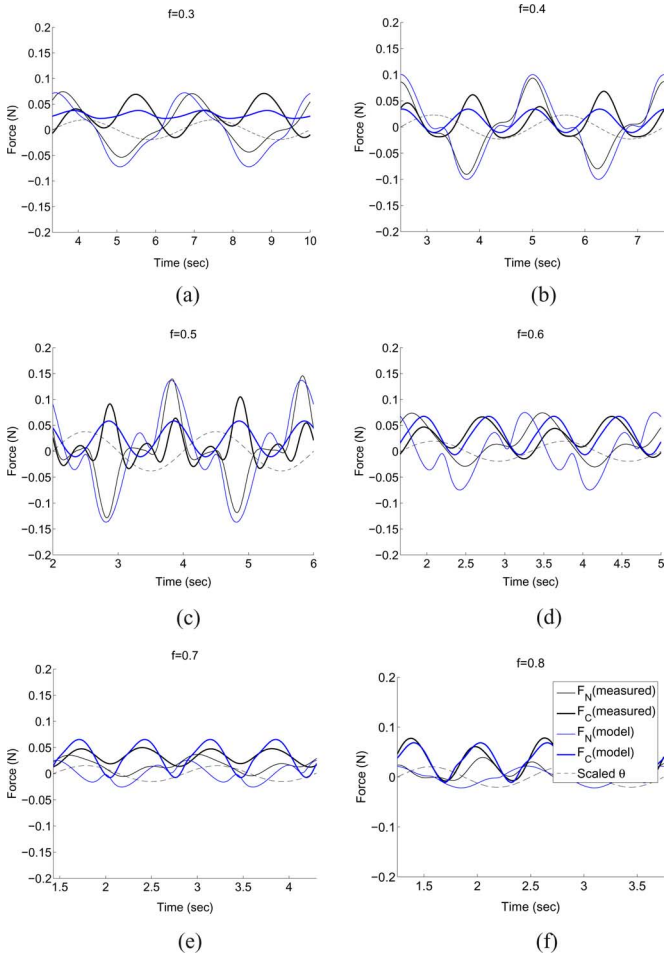

Fig. 10. Model match for the force profiles for the fin: S2 PI at different frequencies. (a) $f = 0.3; C_L = 1, C_D = 0.1$. (b) $f = 0.4; C_L = 1.5, C_D = 0.5$. (c) $f = 0.5; C_L = 1.5, C_D = 0.5$. (d) $f = 0.6; C_L = 0.7, C_D = 0.1, C_{\rm am} = 0.4$. (e) $f = 0.7; C_L = 0.2, C_D = 0.01, C_{\rm am} = 0.1$. (f) $f = 0.8; C_L = 0.1, C_D = 0.2, C_{\rm am} = 0.01$.

C. Fitting the Model to Measured Forces

As mentioned in the previous section, the relative contribution of the normal and chordwise force components varies with frequency for all the shapes. Fig. 10 shows the measured force components of the optimal fin, S2 PI, compared with those calculated from the model in (10) with appropriate values of C_L and C_D. As seen from the figure, for lower frequencies (0.3–0.5 Hz), the normal components from the theoretical and experimental data match very well, while the chordwise components differ considerably. The discrepancy resulted from the flexing of the polyimide fin, and the model is based on the rigid fin assumption, which does not capture the effect of the fin flexibility. At higher frequencies (0.6–0.8), the chordwise components match well, but the normal components dropped in magnitude and could not be matched accurately with the given C_L and C_D values, as a result of flexing. Furthermore, it was found that the added mass contribution had to be reduced with a scaling constant $C_{\rm am}$ from the theoretically predicted added mass force [see (18)]. Flexing of the fin seems to be the only factor that could have resulted in reduced-added-mass effect. Therefore, the current model can only approximate the dominant force generation without considering the fin flexibility effect. Currently, experiments with controlled fin flexibility are being conducted to investigate and model flexible fin hydrodynamics.

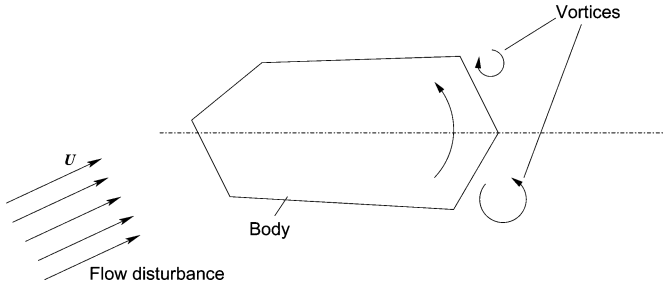

Fig. 11. Schematic showing the desired self-correcting vortex shedding.

PART II: BODY SHAPE DESIGN

This part of the study seeks to understand the role of different morphological parameters that could be responsible for boxfish stability, and transform such findings into engineering design guidelines for the body shape design of a MUV. In this preliminary study, the analysis was performed by using computer-aided design and engineering (CAD/CAE) tools such as solid modeling software and fluid-flow simulation software. First approximate models of boxfish were built in a 3-D modeling software, and the fluid flow was simulated over such models to analyze the vorticity patterns around the body. The relative role of key morphological features like the dorsal and ventral keels, concavity and convexity of the shape, and changes in the cross section along the length of the body were determined. Different MUV body shape designs were built along these lines and tested for the required vortex strength and overall drag to arrive at the best design.

Fig. 11 shows the counter-rotating vortex shedding by a bluff body. The vortex shedding should result in moments that can correct disturbances in the pitch and yaw (not shown in the figure) directions. The shape that can demonstrate this "self-correcting vortex shedding" for pitch and yaw disturbances will be the shape suitable for the body of the MUV.

IV. METHODS AND APPROACH

In order to transform the biological observations concerning the boxfish stability into engineering design guidelines, the morphological features that contribute to the unique vortex shedding patterns (as reported in [11]) had to be identified. Approximate 3-D models capturing essential features of the boxfish were made, and flow at different angles of attack was simulated over such models to study the role of the various features on stability. SolidWorks, a 3-D CAD modeling software was used to build body shapes, and the fluid-flow simulation was carried out using GAMBIT (for defining boundaries of the flow and laying computational grid around the body) and FIDAP (for solving the flow and post processing) of FLUENT, Inc.

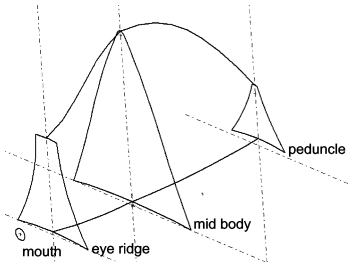

Fig. 12. Cross sections at various planes along the body of the buffalo trunk fish to form the body shape.

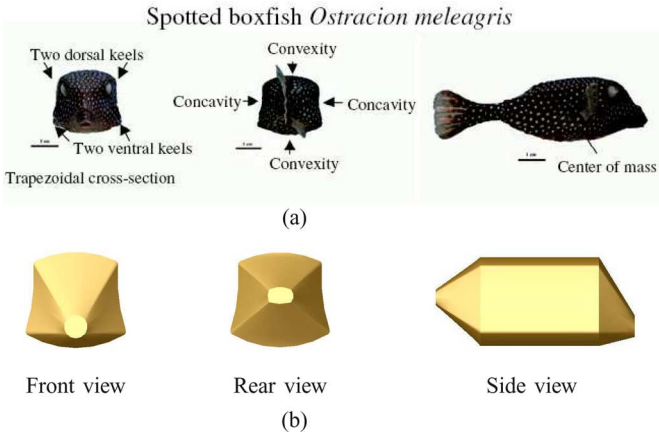

Fig. 13. Spotted boxfish. (a) Planar views of the spotted boxfish considered by Bartol *et al*. in [11]. (b) CAD models.

A. Modeling and Meshing of Boxfish Shapes

3-D models of boxfish were built in SolidWorks. Essential features like dorsal and ventral keels and variation in cross sections along the length of the body were reproduced in the models. Variation of cross section along the body plays a very significant role in the vorticity generation; therefore, cross sections near mouth, eye ridge, peduncle, and any other distinct plane were drawn on 2-D planes and joined to obtain the desired shape. Fig. 12 shows the planes containing important cross sections of the buffalo trunk fish. Only two, the spotted boxfish and the buffalo trunkfish, of the four varieties of boxfish studied in [11] were considered here. The other two shapes are not significantly different from the buffalo trunkfish. Figs. 13(a) and 14(a) show the planar views of the actual boxfish used in the study by Bartol *et al*. 3-D models of the fish used in this study are shown in Figs. 13(b) and 14(b). It has to be noted that the 3-D models were developed based only on the subjective "resemblance," capturing the key features and not accurate measurements of the boxfish morphology.

Once created, the 3-D models were imported into GAMBIT in initial graphics exchange specification (IGES) format. The imported models were then "cleaned" by merging unwanted edges and surfaces that may have hindered mesh generation [35]. To take advantage of the lateral symmetry of the boxfish shape, only (left/right) half of the body was considered for simulation. An external *brick* volume was used for the fluid flow. The symmetry plane of the boxfish was made coincident to one of the brick

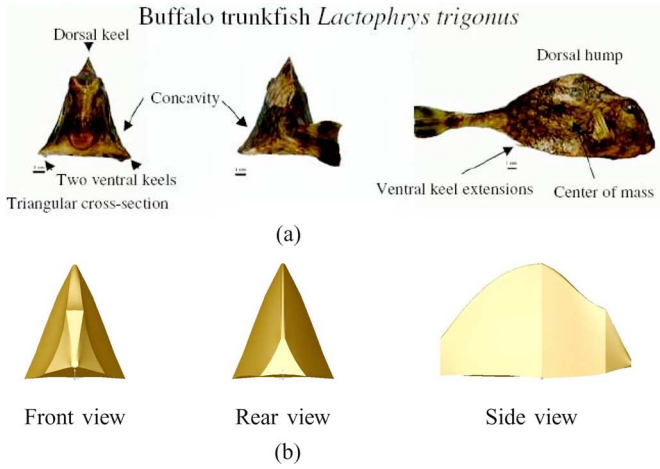

Fig. 14. Buffalo trunkfish. (a) Planar views of the Spotted boxfish considered by Bartol *et al*. in [11]. (b) CAD models.

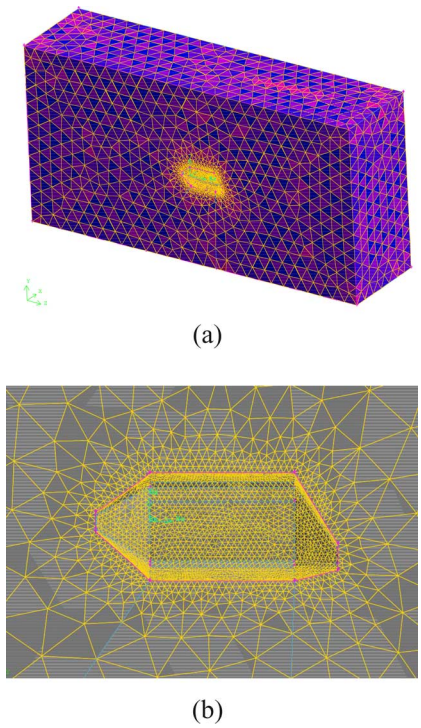

Fig. 15. 3-D mesh generated in the GAMBIT of spotted boxfish. (a) Spotted boxfish shape in the brick volume. The volume separating the brick and the shape is meshed with the finer mesh near the boxfish shape and coarser away from it. (b) Closeup view of the fine mesh around the body shape.

side walls, and the body was placed midway along the height and length of the brick (see Fig. 15). In future simulations, the size of the brick could be increased further to minimize the wall effects. Fig. 15 shows the 3-D mesh generated in the GAMBIT. Shape functions have been defined such that the mesh is finer near the body surfaces and gets coarser away from the body. The mesh size was kept fairly coarse in order to keep the convergence time reasonable. The course mesh was not detrimental to the simulation results because the Reynolds number was only about 300, and thus, did not require a very dense mesh. It has

to be noted that the Reynolds number corresponds to the case where a water wave disturbs an otherwise stationary boxfish, and therefore, is lower than the average Reynolds number of boxfish swimming.

B. Flow Conditions

The flow of constant velocity at various angles of attack was simulated. The Reynolds number for the flow can be defined as

$$\mathrm{Re} = \frac{\rho U L}{\mu} \tag{20}$$

where U is the magnitude of the total velocity vector and L can be taken as the diagonal length along a cross section in case of the spotted boxfish or the height of the largest triangular cross section in case of the buffalo trunkfish.

In order to study the vorticity generation of a body shape, a low Reynolds number flow can be simulated, and the concentration of the vorticity along the sharp features of the body can be analyzed. Thus, the authors have limited the analysis to a very low velocities that result in steady-state laminar flow, and do not require the computational time of an unsteady problem or the fine mesh requirement of turbulent flow. However, some important effects induced by turbulence may be missing in this simulation. In all the flows, the value of U was 1 cm/s, corresponding to a Reynolds number of about 300 for both the fish. The boundary conditions applied were such that the fluid was not allowed to flow through the side, top, and bottom walls of the brick volume enclosing the body shape.

V. Results and Discussion

A. Lessons From Boxfish Stability

Here, the main results and conclusions are summarized and compared to those reported in [11].

First, it was reported in [11] that the ventral keels of all the models produced leading edge vortices (LEVs) that grew in circulation along the bodies, and this was verified in the present study. Vorticity concentration was found at the keel edges for all the models at various cross sections. Vorticity contours at different cross sections for both the fish can be found in [36]. This is expected, as the keels form the sharp corners of the body, and hence, induce the circulation into the oncoming water. However, for a given angle of attack, an increase in the circulation was found only when there is a sudden increase in the cross section. This is true for both the boxfish shapes. For the spotted boxfish in Fig. 16, the maximum concentrated vorticity is located at the eye ridge, where the cross section increases suddenly. Similar behavior was observed for the buffalo trunkfish. The concentrated vorticity near the keels increased along the length until it reached a maximum at the mid body plane, where the body curve attains a peak (Fig. 17).

Second, the present study also verified that vortices formed "above the keels and increased in circulation as pitch angle became more positive, and formed below the keels and increased in circulation as pitch angle became more negative" (verbatim from [11]). Fig. 18 shows the net vertical lift on the spotted boxfish model varying with pitch angle. In [11], the lift coefficients of all the boxfish studied were very near the origin (that is, almost no lift at zero angle of attack). The difference might be error due to the fact that the actual boxfish dimensions were not reproduced in the solid model.

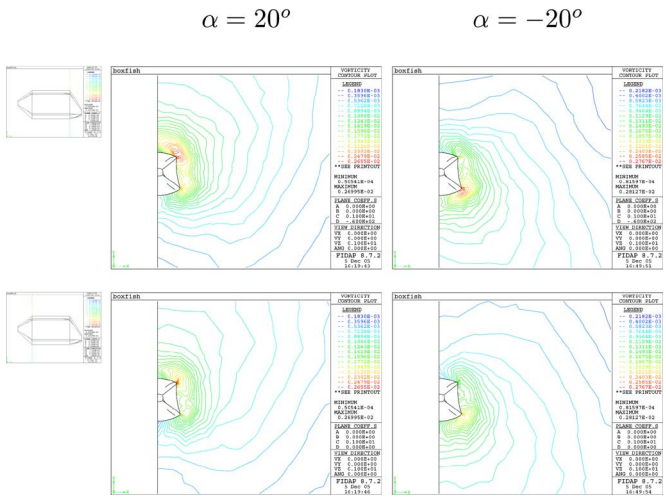

Fig. 16. Vorticity contour maps at various cross sections (as seen from the rear of boxfish) of the *spotted boxfish* for *PITCH* angles of attack $\alpha = 20, -20$.

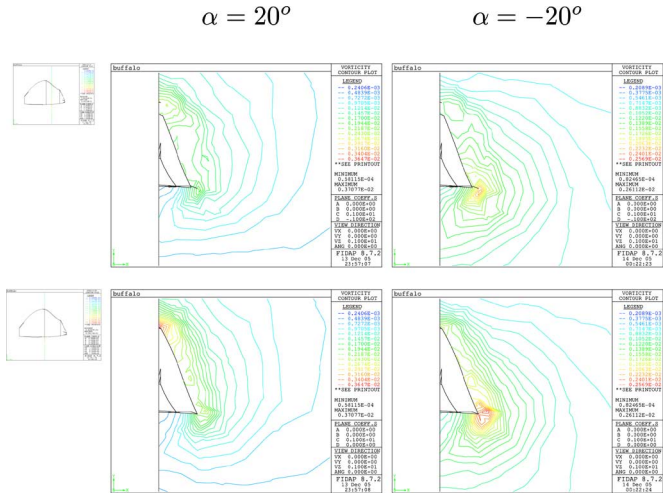

Fig. 17. Vorticity contour maps at various cross sections (as seen from the rear of boxfish) of the *buffalo trunkfish* for *PITCH* angles of attack $\alpha = 20, -20$.

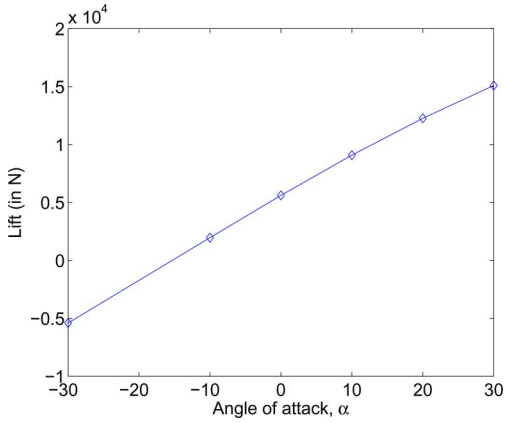

Fig. 18. Overall lift on the spotted boxfish with the pitch angle of attack.

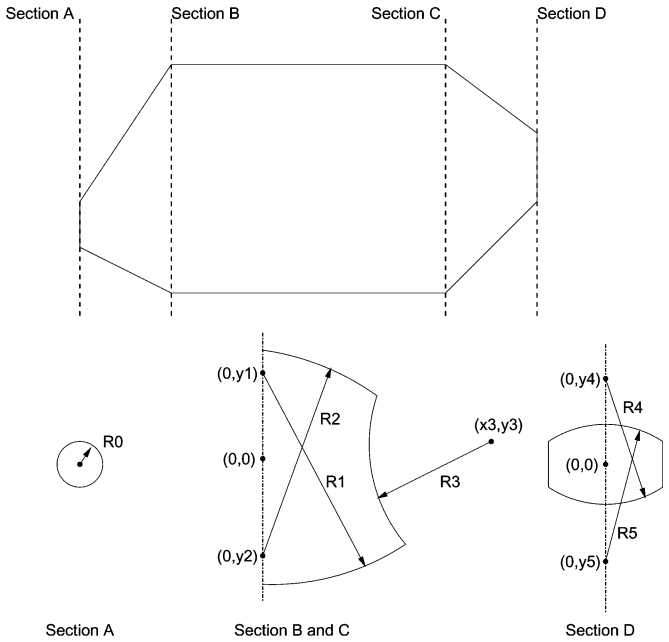

Fig. 19. Shape parameters used to vary the geometry of boxfish like shapes.

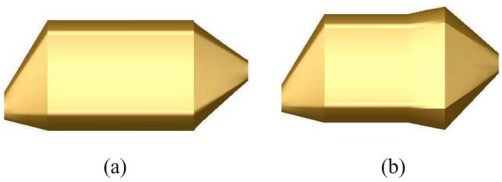

Fig. 20. Shapes considered to study the sudden cross section change. (a) Original shape. (b) With steeper rear bump.

Third, it was found that vortices formed along the eye ridges of all the boxfish: this was clear from the simulation—the eye ridge regions for both the models have shown concentrated vorticity, which, once again, can be attributed to the sudden increase in the cross-section profile.

Finally, when both boxfish were positioned at various yaw angles, regions of stronger concentrated vorticity formed in far-field locations of the carapace when compared with near-field areas, and vortex circulation was greatest in the posterior of center of mass, just as described in [11]. The vorticity contours for the yaw case are not presented here for the sake of brevity and can be found in [36].

B. Toward Underwater Vehicle Shape Design

From the analysis of the actual boxfish like shapes, it has been determined that the following two shape factors are mainly responsible for altering the vortex generating characteristics.

1) Change in the cross-section profile: along the body for pitch stability and across the body for yaw stability.
2) Sharpness of the keels that, in turn, depend on the concavity and convexity of the joining faces.

These two characteristics were explored in the design of the MUV. Fig. 19 shows parameters used to change the body shape of the MUV. In order to verify the first of the two factors (cross-section profile change), the shapes shown in Fig. 20 were considered. Both shapes were modified in the front region, and the rear change of area (the "bump") was increased in the second shape. When the flow was simulated at different pitch angles on both models, the peak vorticity was found to be higher for the second case at all angles of attack, as expected.

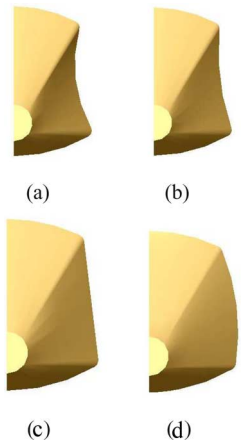

Fig. 21. Shapes with different side surfaces considered to study the keel sharpness. (a) Concave 1. (b) Concave 2. (c) Flat. (d) Convex.

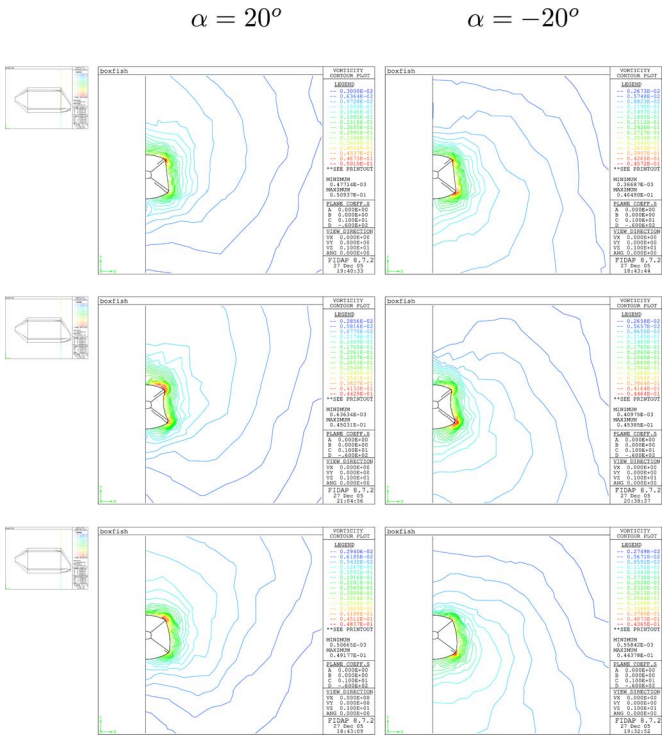

Fig. 22. Vorticity contour maps at front bump cross section (as seen from the rear of boxfish) of *flat, concave, and convex designs* for *PITCH* angles of attack $\alpha = 20, -20$.

The concavity of the side surfaces determines the sharpness of the keel, and hence, can affect the flow separation. To verify this, models with concave, flat, and convex surfaces as shown in Fig. 21 were considered. There was not much variation in the peak vorticity in the simulations for different pitch angles, but the vorticity was concentrated more heavily on the keels of the concave shape than on the flat and convex shapes (see Fig. 22).

For yaw angles of attack, the peak vorticity was higher for the concave design and the vorticity was still concentrated near the keels. A comprehensive set of simulation results can be found in [36].

PART III: ROBOTIC PROTOTYPE

The following section describes the various elements of the robotic prototype design based on the results presented in Part I and II. The robotic boxfish prototype consists of a chassis with flapping units for the pectoral and caudal fins. The outer body shape is rapid prototyped, and assembled on the chassis in left and right halves. It has to be noted that the design objectives of the optimal propulsion and stability have been achieved independently, and the robot design is optimal mainly in the sense of generating propelling force. The fin–body interaction could be of great significance in the overall swimming performance, but has not been investigated in the study presented here.

VI. ROBOT DESIGN ELEMENTS

A. Fin Placement and DOFs

Boxfish employ a total of five fins to maneuver effectively. Biologists have observed three main swimming gaits employed at three different speed levels [9]. The design issue is how many of these fins can be practically implemented in a small underwater vehicle, and how many DOFs are used for each fin motion. For effective planar maneuverability, the DOFs have to be distributed around the body. The present design incorporates a single-DOF flexible tail fin for propulsion, and a pair of 2 DOF pectoral fins for steering (yawing) and diving (pitching). Although the dorsal and anal fins of boxfish are believed to play a role in generating low recoil movement [9] (by canceling the moments induced by other fins), they are not included in the design due to size constraints.

The 2 DOF pectoral fins use flapping and rotational motion in the so-called rowing mode. The rowing mode is a drag-based thrust generation stroke with a full cycle of the fins. The power stroke is a quick backward push of the oil with the chord length perpendicular to the water flow. The recovery stroke involves bringing back the fin with the chord length parallel to the flow. The rotation DOF is used to change the orientation of the fin at stroke reversals. This type of system can generate substantial turning moments about the body center of mass for sharp turns [37]. The pectoral fins can also be used effectively as lifting surfaces by holding them at a suitable angle of attack to an oncoming flow.

B. Mechanisms for Fin Motion

A coaxial wrist mechanism has been designed that is similar to the robotic flapper design presented in [3]. The difference is that there is no deviation in DOF, and the gearbox size has been shrunk to a 2 cm $\times$ 2 cm $\times$ 2 cm volume using the smallest off-the-shelf miter gears available. Fig. 23 shows possible kinematics for the pectoral fin motion. The tail fin mechanism consists of a gear stage between the tail fin shaft and the motor shaft.

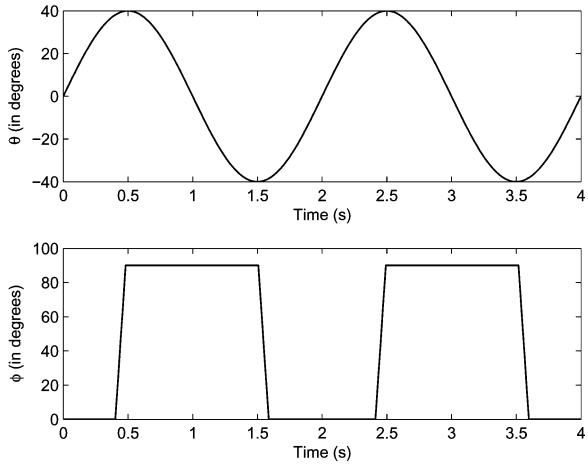

Fig. 23. Flapping and rotation angle functions of time.

TABLE III
ROBOT PARAMETERS

Size and weight			
Length	Width	Height	Weight
15cm	9.2cm	8.5cm	490gm
Fin transmission gear ratios			
G_t^θ	G_t^ϕ	G_w^ϕ	G^ψ
0.75	1.33	1	0.75

The fin kinematics of the robotic boxfish can be described by using relations between the actuator rotation angle and the rotation of the corresponding fin DOF. The side fin flapping and rotation angles are coupled due to the no-slip condition of the wrist bevel gear box. Forward kinematics of the pectoral fin are given by

$$\theta = G_t^\theta G_w^\theta \theta_m \tag{21}$$

$$\phi = G_t^\phi G_w^\phi \phi_m - G_w^\phi \cdot \theta \tag{22}$$

and that of the tail fin simply by

$$\psi = G^\psi \psi_m \tag{23}$$

where Gs are appropriate gear ratios. The robot size parameters and the gear ratios can be found in Table III. Subscripts t and w indicate the top plate and the wrist mechanism, and superscripts indicate the DOF angle.

C. Chassis Design

The pectoral fin mechanism required the motors driving it to be placed above the wrist mechanism. A parallel plate structure was used to place the pectoral fin motors in front and above the wrist gear box (see Fig. 24 for chassis structure). The electronic chips were placed on the top plate along with the pectoral fin motors and the transmission mechanism. The battery pack, tail fin motor, and transmission were mounted on the bottom plate. The plates are made out of 0.125-in-thick delrin sheet. A computer numerical control (CNC) mill was programmed to machine all the features on the plates.

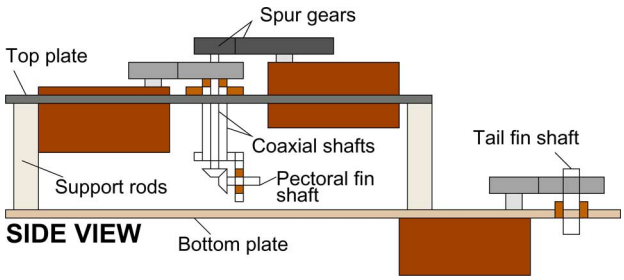

Fig. 24. MUV chassis.

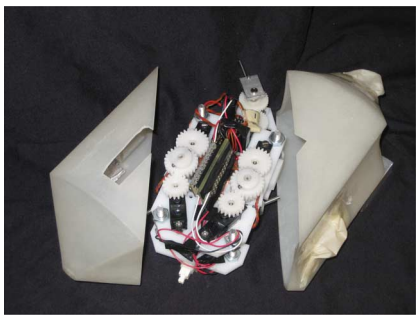

Fig. 25. Latest MARCO configuration with body shape mounted using diagonal halves for better sealing of the tail fin, which is now entirely covered with the right half.

D. Actuators and Electronics

The actuator selection was one of the most important factors governing the size of the MUV. The accurate positioning of the fin flapping angles was required to control the force generation for turning and cruising. Servo motors with built-in feedback were used in place of a dc motor and the encoder combination. All the servos are daisy-chained to a servo controller that drives them to the position commanded by the processor.

The onboard electronics include a Javelin–Stamp microprocessor module by Parallax, Inc., and a serial motor controller printed circuit board (PCB) unit by Pololu, Inc. The power supply for the motors, motor controller, and processor is provided by a pack of five 1.2 V NiMH batteries. The microprocessor was programmed using an embedded Java version. A Java class routine was used to command the motor controller in a serial communication mode using a built-in UART object. The object class files for different sensors could be easily incorporated into the program.

E. Outer Shape

The outer shape of the MUV was rapid prototyped using the stereolithograhy (3-D printing) technique. Features for assembly and fin placement were incorporated into the shape. To seal the robot, layers of adhesive tape and oil resistant film were applied along the dividing line between the two body halves. The fin extensions were covered with a latex sheet and attached to the shaft with a plastic O-ring. The latest configuration of the robot is one in which the body shape is assembled in diagonal halves, as shown in Fig. 25. This makes sealing the tail fin easier as compared to the earlier version, where the tail fin sealing and the robot body sealing have to be done in the same area. Fig. 26 shows the swimming prototype.

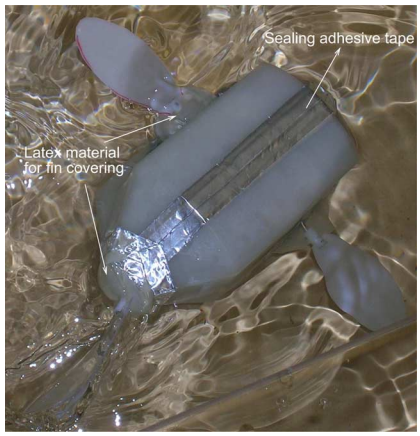

Fig. 26. Swimming prototype.

F. Buoyancy and Center of Mass

For the robot to be neutrally buoyant, the weight force must be equal to the buoyancy force. The buoyancy is determined by the volume of oil (experimental trials were conducted in a low viscosity, clear oil to avoid electrical shorting) displaced by the solid model. Copper bars, machined to fit underneath the chassis plates, were used to balance the buoyancy force and the weight force. The heaviest parts, such as the batteries and large copper plate, were designed to fit in the lower region of the MARCO. By placing the center of mass below the center of buoyancy, the robot was designed to have inherent stability. The location of the center of mass was found by hanging the prototype from a string attached at different points and taking an image. The images were overlaid on top of one another, and a line was drawn to extend the line of the string. The approximate point of intersection of all the lines was the experimental center of mass.

VII. Experimental Trials

The current robotic prototype can be programmed to use different gait styles. A charge-coupled device (CCD) camera, by Allied Vision Technology, operating at 30 ft/s was used to record swimming trials and determine the speed, recoil movement, and turning radius. The robot was run in the field of view of the camera, and each image was saved in the National Instrument's Vision Assistant for LabVIEW. A virtual instrument (VI) was created to calibrate the pixels to real world units of inches. Each image was then sequentially analyzed for the speed, recoil, and turning radius. The speed and turning radius were measured by the change in position of a point on the robot and a constant point in the field of view. The average speed obtained was 0.0411 m/s, with an almost zero turning radius. The recoil can be measured by the deviation in each frame from the straight line between the beginning and end points. The average recoil was found to be 0.826 cm. The gait used for the test is shown in Fig. 27.

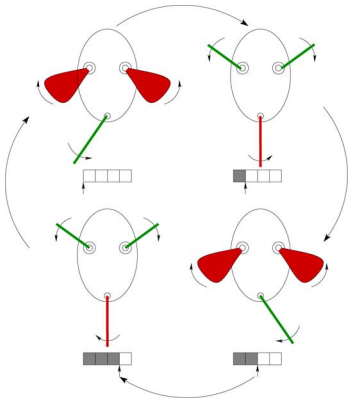

Fig. 27. Gait used for forward motion.

The green color of the fins indicates the phase of the stroke where the forward propulsive thrust is produced, and the red color indicates the phase where the force generated is either minimal (like the recovery stroke of the pectoral fin) or in the direction opposite to the motion of the robot (as in the case of the caudal fin). The gait in Fig. 27 is one where a constant forward propulsive force is applied to the body during most of the caudal fin cycle.

VIII. Conclusion and Future Work

In this paper, we present the research leading to the design of a biologically inspired robotic ostraciiform MARCO. The design attempts to achieve the maneuverability of a small scale, multiple fin underwater system like that of the boxfish, while also incorporating a body with a self-correcting mechanism.

Experimental studies were conducted to characterize and optimize the flapping fin propulsion of the tail fin. Toward this, a 3 DOF robotic flapper was designed to act as the flapping tail or side fin of the fish, and a fixed-beam-based force sensor was designed to measure the instantaneous forces generated by the fin motion. A tail fin with optimal-shape-induced flexibility has been found. The hydrodynamic force generation of tail fin has been modeled using a combination of quasi-steady lift generation, and empirically found drag and added mass effects. Fluid flow simulations on 3-D CAD models of boxfish-like shapes were used to arrive at the outer shape of the MUV. A robotic prototype of the MUV was designed based on the earlier analysis. The propulsion and maneuvering of the MUV is achieved by the tail fin and two 2 DOF side fins.

One of the immediate goals is to use the prototype to evaluate the efficiency of various gait patterns for a given set of flow conditions. Sensors and command architecture will also be used in future generations to give the robot greater autonomy. Currently, new mechanical sealing techniques and more processing power are being incorporated into the next generation of the prototype to facilitate longer trial runs and effective control of the robot. Studying fin–fin and body–fin interactions can help modify the design of the body shape and/or fin kinematics for optimal thrust production or even better maneuverability. One such problem is that of the interaction between the side fin and tail fin. On a small robot like the present MUV, the proximity of the side fin and the tail fin is more and can lead to strong interactions between them. Such mechanisms can be investigated by using multiple flappers and/or body shape in the tow tank. Recent experimental studies on dragonfly forewing–hindwing interaction [38] and insect wing–wing interaction [39] can be seen for further reference.

References

[1] J. Yuh, "Design and control of autonomous underwater robots: A survey," *Auton. Robots*, vol. 8, pp. 7–24, 2000.

[2] P. Kodati, J. Hinkle, and X. Deng, "Micro autonomous robotic ostraciiform (MARCO): Design and fabrication," in *Proc. IEEE Int. Conf. Robot. Autom. (ICRA)*, Apr. 10–14, 2007, pp. 960–965.

[3] P. Kodati and X. Deng, "Experimental studies on the hydrodynamics of a robotic ostraciiform tail fin," in *Proc. IEEE/RSJ Int. Conf. Intell. Robots Syst. (IROS)*, Oct. 2006, pp. 5418–5423.

[4] P. Kodati and X. Deng, "Towards the body shape design of a hydrodynamically stable robotic boxfish," in *Proc. IEEE/RSJ Int. Conf. Intell. Robots Syst. (IROS)*, Oct. 2006, pp. 5412–5417.

[5] M. Sfakiotakis, D. M. Lane, and J. B. C. Davies, "Review of fish swimming modes for aquatic locomotion," *IEEE J. Ocean. Eng.*, vol. 24, no. 2, pp. 237–252, Apr. 1999.

[6] C. C. Lindsey, "Form, function and locomotory habits in fish," in *Fish Physiology Volume VII: Locomotion*, W. S. Hoar and D. J. Randall, Eds.. New York: Academic, 1978, pp. 1–100.

[7] J. E. Colgate and K. M. Lynch, "Mechanics and control of swimming: A review," *IEEE J. Ocean. Eng.*, vol. 29, no. 3, pp. 660–673, Jul. 2004.

[8] C. M. Breder, "The locomotion of fishes," *Zoologica*, vol. 4, pp. 159–256, 1926.

[9] M. Gordon, J. Hove, P. Webb, and D. Weihs, "Boxfishes as unusually well-controlled autonomous underwater vehicles," *Physiol. Biochem. Zool.*, vol. 74, no. 6, pp. 663–671, 2000.

[10] I. K. Bartol, M. Gharib, D. Weihs, P. W. Webb, J. R. Hove, and M. S. Gordon, "Hydrodynamic stability of swimming in ostraciid fishes: Role of the carapace in the smooth trunkfish lactophrys triqueter," *J. Exp. Biol.*, vol. 206, no. 4, 2003.

[11] I. K. Bartol, M. Gharib, P. W. Webb, D. Weihs, and M. S. Gordon, "Body-induced vortical flows: A common mechanism for self-corrective trimming control in boxfishes," *J. Exp. Biol.*, vol. 208, pp. 327–344, 2005.

[12] M. S. Triantafyllou and G. S. Triantafyllou, "An efficient swimming machine," *Sci. Am.*, vol. 272, no. 3, 1995.

[13] D. S. Barrett, M. S. Triantafyllou, D. K. P. Yue, M. A. Grosenbaugh, and M. J. Wolfgang, "Drag reduction in fish-like locomotion," *J. Fluid Mech.*, vol. 392, pp. 183–212, 1999.

[14] Q. Zhu, M. J. Wolfgang, D. K. P. Yue, and M. S. Triantafyllou, "Three-dimensional flow structures and vorticity control in fish-like swimming," *J. Fluid Mech.*, vol. 468, pp. 1–28, Oct. 2002.

[15] G. L. J. Authors Liao, D. N. Beal, and M. Triantafyllou, "Fish exploiting vortices decrease muscle activity," *Science*, vol. 302, pp. 1566–1569, 2003.

[16] K. A. McIsaac and J. P. Ostrowski, "Motion planning for anguilliform locomotion," *IEEE Trans. Robot. Autom.*, vol. 19, no. 4, pp. 637–652, Aug. 2003.

[17] M. A. MacIver, E. Fontaine, and J. W. Burdick, "Designing future underwater vehicles: Principles and mechanisms of the weakly electric fish," *IEEE J. Ocean. Eng.*, vol. 29, no. 3, pp. 651–659, Jul. 2004.

[18] M. Epstein, J. E. Colgate, and M. A. MacIver, "Generating thrust with a biologically-inspired robotic ribbon fin," presented at the IEEE/RSJ Int. Conf. Intell. Robots Syst. (IROS), Beijing, China, 2006.

[19] D. Lachat, A. Crespi, and A. J. Ijspeert, "Boxybot: A swimming and crawling fish robot controlled by a central pattern generator," in *Proc. first IEEE/RAS-EMBS Int. Conf. Biomed. Robot. Biomechatron. (BioRob 2006)*, pp. 643–648.

[20] J. P. S. Floyd, T. Keegan, and M. Sitti, "A novel water running robot inspired by basilisk lizards," in *Proc. IEEE/RSJ Int. Conf. Intell. Robots Syst. (IROS)*, Oct. 2006, pp. 5430–5436.

[21] S. Licht, V. Polidoro, M. Flores, F. S. Hover, and M. S. Triantafyllou, "Design and projected performance of a flapping foil AUV," *IEEE J. Ocean. Eng.*, vol. 29, no. 3, pp. 786–794, July 2004.

[22] F. E. Fish, G. V. Lauder, R. Mittal, A. H. Techet, M. S. Triantafyllou, J. A. Walker, and P. W. Webb, "Conceptual design for the construction

of a biorobotic AUV based on biological hydrodynamics," in *Proc. 13th Int. Symp. Unmanned Untethered Submersible Technology,* Autonomous Undersea Systems Institute, Durham, NH, 2003.
[23] K. Mohseni, "Zero-mass pulsatile jets for unmanned underwater vehicle maneuvering," presented at the AIAA 3rd Unmanned Unlimited Tech. Conf., Workshop Exhibit, Chicago, IL, Sep. 2004.
[24] B. S. Y. Kato and N. Wicaksono, "Development of biology-inspired autonomous underwater vehicle bass iii with high maneuverability," in *Proc. 2000 Int. Symp. Underwater Technol.*, 2000, pp. 84–89.
[25] P. R. Bandyopadhyay, "Trends in biorobotic autonomous undersea vehicles," *IEEE J. Ocean. Eng.*, vol. 30, no. 1, pp. 109–139, Jan. 2005.
[26] M. S. Triantafyllou, G. S. Triantafyllou, and R. Gopalkrishnan, "Wake mechanics for thrust generation in oscillating foils," *Phys. Fluids A*, vol. 3, no. 12, pp. 2835–2837, 1991.
[27] P. Prempraneerach, F. Hover, and M. S. Triantafyllou, "The effect of chordwise flexibility on the thrust and efficiency of a flapping foil," in *Proc. Int. Symp. Unmanned Untethered Submersible Technol.*, 2003.
[28] N. Kato and H. Liu, "Optimization of motion of a mechanical pectoral fin," *JSME Int. J., Series C*, vol. 46, no. 4, pp. 274–279, 2003.
[29] J. A. Walker and M. W. Westneat, "Kinematics, dynamics, and energetics of rowing and flapping propulsion in fishes," *Integr. Comp. Biol.*, vol. 42, pp. 1032–1043, 2002.
[30] M. S. Triantafyllou, A. H. Techet, and F. S. Hover, "Review of experimental work in biomimetic foils," *IEEE J. Ocean. Eng.*, vol. 29, no. 3, pp. 585–594, Jul. 2004.
[31] M. H. Dickinson, F. O. Lehmann, and S. S. Sane, "Wing rotation and the aerodynamic basis of insect flight," *Science*, vol. 284, no. 5422, pp. 1954–1960, 1999.
[32] S. Combes and T. Daniel, "Flexural stiffness in insect wings. II. Spatial distribution and dynamic wing bending," *J. Exp. Biol.*, vol. 206, no. 17, pp. 2979–2987, 2003.
[33] K. Karamcheti, *Principles of Ideal Fluid Aerodynamics*. New York: Dover.
[34] L. I. Sedov, *Two-Dimensional Problems in Hydrodynamics and Aerodynamics*. New York: Interscience, 1965.
[35] *GAMBIT 2.1 Tutorial Manual*, FLUENT Inc., Lebanon, NH, 2003.
[36] P. Kodati, "Biomimetic micro underwater vehicle with ostraciiform locomotion: System design, analysis and experiments" Master's thesis, Univ. Delaware, Newark, Aug. 2006.
[37] J. A. Walker, "Does a rigid body limit manuerability?," *J. Exp. Biol.*, vol. 203, pp. 3391–3396, 2000.
[38] W. J. Maybury and F.-O. Lehmann, "The fluid dynamics of flight control by kinematic phase lag variation between two robotic insect wings," *J. Exp. Biol.*, vol. 207, pp. 4707–4726, 2004.
[39] F. O. Lehmann, S. P. Sane, and M. H. Dickinson, "The aerodynamic effects of wing-wing interactions in flapping insects," *J. Exp. Biol.*, vol. 208, pp. 3075–3092, 2005.

Parasar Kodati received the B.Tech. degree from the Indian Institute of Technology, Guwahati, Assam, India, in 2003, and the M.S. degree from the University of Delaware, Newark, in 2006, both in mechanical engineering.

He is currently an Application Support Engineer at the Mathworks, Natick, MA, where he is engaged in control design automation products. Prior to joining The Mathworks, he was an Associate Engineer at Dade Behring (now part of Siemens Medical Solutions Diagnostics), Newark, DE. During 2001, he was involved in robotics research as an intern at the Bhabha Atomic Research Center, Mumbai, India and at the National University of Singapore, Singapore, during 2002. He was a Noise and Vibration engineer at the TVS Motor Company, Hosur, India, before joining the University of Delaware as a graduate student in 2004. His current research interests include engineering product design and development with emphasis on modeling, simulation, and control of mechanical systems.

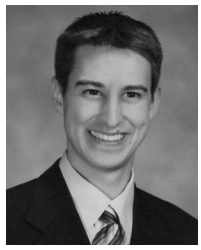

Jonathan Hinkle received the B.S. degree in mechanical engineering with specialization in aerospace engineering from the University of Delaware, Newark, in 2007.

He is currently an Aerospace Design Engineer at the International Linear Collider (ILC), Dover, DE. His current projects include the Orion Crew Exploration Vehicle (CEV) landing system and lunar habitat modules both in conjunction with the National Aeronautics and Space Administration (NASA) Langley Research Center.

Aaron Winn received the B.S. degree (honors) in mechanical engineering with specialization in aerospace engineering from the University of Delaware, Newark, in 2007.

He is currently a Design Engineer at GE Energy Gas Turbines. His current research interests include aerodynamics, heat transfer, design of thermomechanical systems, and advanced modeling.

Xinyan Deng received the B.S. degree in automation from Tianjin University, Tianjin, R.O.C., in 1995, and the Ph.D. degree in mechanical engineering from the University of California, Berkeley, in 2004.

Since 2004, she has been an Assistant Professor in the Department of Mechanical Engineering, University of Delaware (UD), Newark, and the Director of the Microrobotics Laboratory at UD. Her current research interests include biomimetic microrobots, microaerial vehicles and underwater vehicles, bioinspired sensors, control of biomimetic locomotion, modeling, and simulation of biological systems.